We are IntechOpen, the world's leading publisher of Open Access books Built by scientists, for scientists

4,800
Open access books available

122,000
International authors and editors

135M
Downloads

Our authors are among the

154
Countries delivered to

TOP 1%
most cited scientists

12.2%
Contributors from top 500 universities

WEB OF SCIENCE™

Selection of our books indexed in the Book Citation Index in Web of Science™ Core Collection (BKCI)

Interested in publishing with us?
Contact book.department@intechopen.com

Numbers displayed above are based on latest data collected.
For more information visit www.intechopen.com

19

Steel Building Assessment in Post-Earthquake Fire Environments with Fiber Optical Sensors

Genda Chen, Ying Huang and Hai Xiao
Missouri University of Science and Technology
Untied States of America

1. Introduction

This chapter is aimed to develop and calibrate a quasi-distributed optical sensor network of long period fiber gratings and extrinsic Fabry-Perot interferometers for simultaneous high temperature and large strain measurements, and to validate it for the post-earthquake assessment of a steel frame in high temperature environments. The steel frame represents typical steel buildings that are susceptible to the high temperature effect of earthquake-induced fires such as those observed at multiple locations during the March 11, 2011, Japan earthquake.

Critical buildings such as hospitals and police stations must remain functional for post-earthquake responses and evacuation immediately following a major earthquake event. However, they often experience large strains due to shaking effects as observed during recent earthquakes, causing permanent inelastic deformation. The post-earthquake fires associated with the earthquake-induced short fuse of electrical systems and leakage of gas devices can further strain the already damaged structures during the earthquakes, potentially leading to a progressive collapse of buildings. In a matter of seconds to an hour, tenants can be injured and trapped in the collapsed buildings, desperately waiting for rescue in helpless situations. Therefore, real time monitoring and assessment of the structural condition of critical buildings is of paramount importance to post-earthquake responses and evacuation in earthquake-prone regions. An accurate assessment of the buildings in these harsh conditions can assist fire fighters in their rescue efforts and save earthquake victims.

For structural condition assessment in fire environments, the most widely used, commercial sensing tools are based on electrical principles, including electrical resistance gauges for strain measurements and thermocouples for temperature measurements. Electrical resistance gauges were initially proposed in 1856 by Lord Kelvin (Thomson 1857). A strain gauge is basically a conductive metal foil that is printed on a non-conductive insulating flexible backing. It can be applied to the surface of a solid structure with suitable adhesives, such as cyanoacrylate. When perfectly attached, the foil and then the backing are deformed together with the structure to be monitored, causing a change in electrical resistance of the alloy. Due to electromechanical properties of the alloy, the foil and the adhesives, the maximum strain that a strain gauge can measure prior to its failure is typically limited to 1%. The readings from a strain gauge also vary with the temperature during measurements. They become significant in high temperature applications and must be compensated for temperature effects.

For strain measurements in high temperature environments, significant improvements on the temperature properties of strain gauges were made by Easerling (1963) and Gregory et al. (2007). Commercial products introduced by Vichy Micro-Measurement can be applied to measure a strain of *5,000 με* at *1,000˚F*. However, wired strain gauges would likely lose their signals due to power outage during and immediately following a strong earthquake when structures being monitored are subjected to large strains and post-earthquake fire environments. For the same reason, conductive textiles that are operated with their electromechanical properties through a special design of "sensing string" will likely be malfunctional even though the sensors can be used for large strain measurements (Zhang 2006).

For temperature measurements, thermocouples were initially proposed in 1822 by Fourier and Oersted, and based on the thermoelectricity principle discovered by Thomas in 1821 (ASTM 1981). Since then, thermocouples have been widely used for high temperature measurements. Today, a variety of thermocouples are commercially available for various temperature ranges, including Type K, E, J, N, B, R, S, T, C, and M. A thermocouple is a device consisting of two different conductors (usually metal alloys) that produce a voltage proportional to a temperature difference between either ends of the pair of conductors. The change in voltage corresponds to the temperature to be measured. Like strain gauges, the measured voltage change and then the converted temperature may not be able to be transferred to a central data acquisition in post-earthquake fire environments.

The above review clearly indicates that a conventional monitoring system with strain gauges and thermocouples is inadequate for structural condition assessment in harsh environments, such as extremely high temperature in the event of a post-earthquake fire. On the other hand, an optical fiber monitoring system can provide a viable means for this application. In addition to its high temperature tolerance, optical fibers are compact, immune to electromagnetic interference, durable in acid environment, and capable of being integrated into various types of structures and materials. Once developed for large strain measurement capabilities, optical fiber sensors can be multiplexed and integrated into a quasi-distributed, multi-parameter sensing network in harsh environments.

Various fiber optical sensors have been developed mainly based on the intensity changes, gratings, and interferometers with the last two most widely investigated. Grating based optical sensors are led by the fiber Bragg grating (FBG) and the long period fiber grating (LPFG) technologies. A FBG sensor couples two light beams in their respective forward- and backward-propagating core-guided modes near a resonant wavelength, functioning like a wavelength-selective mirror (Othonos 1999). A LPFG sensor with a periodic refractive index perturbation of its fiber core has a period of the hundreds of micrometer and couples the core mode (guided light inside the core of the fiber) into the cladding modes at certain discrete wavelengths (known as resonance wavelengths) (Vengsarkar et al. 1996). For strain measurements at high temperatures, FBG sensors were applied by Wnuk et al. (2005) and Mateus et al. (2007); LPFG sensors were investigated by Huang et al. (2010a). In addition, extrinsic Fabry-Perot interferometer (EFPI) sensors were developed both for a small range of strain measurement (Xiao et al. 1997) and for a large range of strain measurement (Huang et al. 2010b, 2011). However, fiber optical sensors for large strain measurements at high temperature are yet to be studied. Furthermore, their applications for structural behaviour monitoring in post-earthquake fire environments have not been investigated.

In this chapter, an EFPI-based sensor is first introduced and characterized for large strain measurements with high resolution. In particular, the operational principle, signal processing algorithm, and experimental validation of the EFPI sensor are investigated in detail. The EFPI sensor developed for large strain measurements is then combined with a LPFG-based temperature sensor for simultaneous large strain and high temperature measurements. A straightforward signal decomposition technique is introduced for the evaluation of temperature and strain from the readings of an EFPI-LPFG sensor. Lastly, the developed fiber optical sensors are multiplexed in an optical fiber sensing network and validated in their application to a steel frame under a simulated post-earthquake fire environment for structural behaviour monitoring and assessment.

2. An EFPI based large strain sensor with high resolution

An EFPI sensor can be made by first inserting two cleaved optical fibers into a capillary tube and then bonding them to the tube with epoxy or in thermo fusion. This way of packaging improves the sensor's robustness in applications, but limits the sensor's dynamic range to the corresponding maximum deformation of the capillary tube. On the other hand, if the two cleaved ends are left unattached to the tube, the packaged device is essentially a displacement sensor. By dividing the measured displacement by the initial distance between the two cleaved ends, the device can be implemented as a large strain sensor. For example, if one or two ends of the fibers are adhered to a substructure to be monitored, the packaged device will experience an applied strain that can be determined from the measured displacement by the EFPI as the substructure deforms under an external load. In this case, the technological challenge remains in achieving high resolution during a large strain measurement. The concept of movable EFPI sensors was developed by Habel et al. (1996) and applied for strain measurements during the first few hours of hydration reaction in concrete (Habel et al. 1996, 1997, 2008).

Up to date, most applications of movable EFPI sensors deal with strain measurements in small range. The resolution of the sensors for large strain measurement has not been analysed systematically. Over the past twenty years, several data processing methods have been investigated to analyse data series from EFPI sensors in structural health monitoring applications (Liu et al. 2001 and Qi et al. 2003). Due to a small range of strain measurement, the so-called phase tracking method with relatively high resolution has been widely applied. Qi et al. (2003) developed a hybrid data processing method by combining several methods using a white light interferometer. Although only tested for a small dynamic range in strain measurements, the data processing technique appears to be a promising concept that can be extended to achieve an increasing dynamic range and resolution with EFPI sensors.

2.1 Operational principle

2.1.1 Sensor structure and measurement system

Fig. 1 shows the schematic of an EFPI sensor head and its associated measurement system. As illustrated by the enlarged view of the sensor head in Fig. 1(a), the EFPI is formed by two perpendicularly cleaved end faces of a single-mode optical fiber (Corning SMF-28). The left side of the fiber serves as a lead-in fiber and the right side serves as a low reflective mirror.

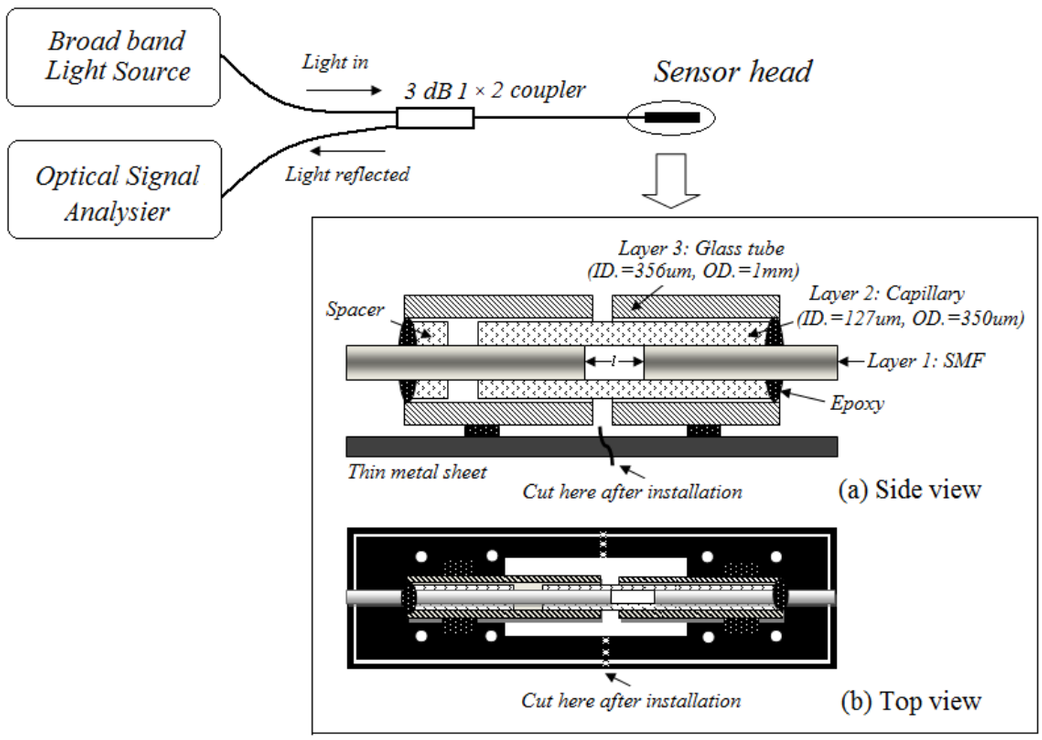

Fig. 1. Schematic of an EFPI sensor: sensor structure and measurement system

In theory, a Fabry-Perot cavity with a freely movable end face can be constructed by inserting two cleaved fiber ends into the two ends of a glass tube and gluing one side of the bare fiber to the tube. However, the freely movable bare fiber end, when not glued to the tube, is easy to break in applications since optical fibers are susceptible to any shear action. To address this issue, a three layer structure is used to package an EFPI strain sensor, including an inner, intermediate and outer layer. The inner layer or Layer 1 in Fig. 1(a) is an optical glass fiber of *125 μm* in diameter. The intermediate layer or Layer 2 in Fig. 1(a) is a capillary glass tube with an inside diameter of *127 μm* and an outside diameter of *350 μm*. The capillary tube is designed to guide the cleaved fiber to ensure that its two end faces can move in parallel. The outer layer or Layer 3 in Fig. 1(a) is a glass tube with an inside diameter of *356 μm* and an outside diameter of *1,000 μm*, which is designed to enhance the overall stability of the packaged sensor. On one side (right) of the interferometer, all three layers are bonded together with epoxy as illustrated in Fig. 1(a). On the other side (left), the fiber is bonded to the third layer through an inserted spacer while the intermediate layer is unbounded to allow for free movement of the fiber end faces within the capillary tube.

The three-layer structure transfers a shear force from the bare fiber to the intermediate layer (spacer) during operation. As its diameter increases, the intermediate layer is less susceptible to the applied shear force so that the proposed structure can operate stably without breakage. The two pieces of the outer glass tube are bonded to a thin metal sheet both at the lead-in side and mirror side of the fiber sensor. The metal sheet has two perforated side strips and a pre-cut rectangular hole in the middle section. It can be bolted to a steel substructure in applications as illustrated in Fig. 1(b). The sensor installation is completed by cutting the two side strips across the perforation of the thin metal sheet. The

separation of the attachment sheet ensures that the sensor actually measures the elongation of the steel substructure between the two sides of the cut section as clearly illustrated in the top view of Fig. 1(b). The distance between the two bolts closest to the cut section is defined as the gauge length of the sensor, which is $L = 2\ mm$ in this study. The EFPI cavity length is designated as l. Based on the proposed sensor structure, a sensor prototype was fabricated as shown in Fig. 2(a) and the micro-view of its sensor head can be seen in Fig. 2(b).

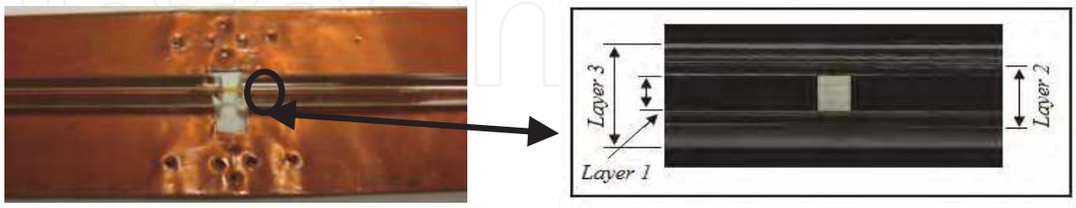

(a) Top view of a sensor prototype: sensor head and metal attachment sheet

(b) Side view of the sensor head taken with an optical microscope

Fig. 2. Sensor prototype

As shown in Fig. 1, the measurement system of an EFPI sensor uses a broadband light source (BBS) of wavelength from *1520 nm* to *1620 nm*, which is generated by multiplexing a C-band (BBS 1550A-TS) and an L-band (HWT-BS-L-P-FC/UPC-B) Erbium Doped fiber amplified spontaneous emission (ASE). The light propagates into the EFPI sensor through a *3 dB* coupler. As the light travels through the lead-in fiber, part of the light is reflected at both cleaved end faces of the EFPI sensor, producing a backward travelling interference signal. The reflected interference spectrum coupled back by the coupler is detected by an optical spectrum analyzer (OSA, HP 70952B). A personal computer is used to record and process the interference spectra. Finally, the characteristic wavelength on the spectrum can be related to the cavity of the EFPI or the strain applied to the substructure in various resolutions with the signal processing algorithms presented in Section 2.1.2.

2.1.2 Signal processing algorithms

To simultaneously achieve a large dynamic range and high resolution in strain measurements, three data processing methods are introduced and studied to characterize their performance. These methods include 1) interference frequency tracking of the Fourier transform of a spectral interferogram, 2) period tracking and 3) phase tracking of the spectral interferogram.

Interference Frequency Tracking Method A low finesse EFPI can generally be modelled by a two-beam interference theory (Taylor 2008). The spectral interferogram of an EFPI typically represents a harmonic function of wavenumber with a dominant frequency known as the interference frequency. By taking the Fourier transform of such an interferogram, an approximate delta function of cavity length corresponding to the interference frequency is obtained (Liu et al. 2000). The cavity length of the EFPI, l, can then be calculated by Equation 1:

$$l = \frac{n\pi}{\left(v_E - v_S\right)} \tag{1}$$

in which v_S and v_E are the wavenumbers of the start and end points of an observation bandwidth, respectively, and n is an integer representing the Fourier series index.
It can easily be observed from Equation 1 that the minimum detectable cavity length change of an EFPI large strain sensor is $\pi/(v_E - v_S)$ when $n=1$. For a light source with a spectrum width of *100 nm*, the detectable cavity length change is approximately *12 μm*. This corresponds to strain resolution of approximately *6,000 με* when a gauge length of *2 mm* is used. As indicated by Equation 1, the strain resolution is inversely proportional to the bandwidth of the light source. Higher resolution in strain measurement thus requires an optical source with a broader bandwidth, which can only be provided by a limited selection of equipment available in the market.
Period Tracking Method Due to the interrelation between period and interference frequency, the change in period of the spectral interferogram can also be used to determine the cavity length of an EFPI (Taylor 2008). The period of a spectral interferogram is defined as the distance between two consecutive valleys on the spectral interferogram. By introducing a wavenumber-wavelength relation ($\nu = 2\pi / \lambda$), the cavity length can be evaluated by Equation 2:

$$l = \frac{\lambda_1 \lambda_2}{2(\lambda_2 - \lambda_1)} \tag{2}$$

where λ_1 and λ_2 ($\lambda_2 > \lambda_1$) represent the first and second wavelengths of two consecutive valleys on the spectral interferogram that can be directly taken from OSA measurements.
Let S_l be the resolution of a strain sensor, which is defined as the minimum detectable change in cavity length when using the period tracing method. Therefore, when λ_1 and λ_2 are assumed to be two independent random variables, S_l can be derived from Equation 2 and expressed into Equation 3:

$$S_l = \sqrt{(\frac{\partial l}{\partial \lambda_1})^2 (S_{\lambda_1})^2 + (\frac{\partial l}{\partial \lambda_2})^2 (S_{\lambda_2})^2} = \sqrt{\frac{{\lambda_2}^4}{4(\lambda_2 - \lambda_1)^4} (S_{\lambda_1})^2 + \frac{{\lambda_1}^4}{4(\lambda_2 - \lambda_1)^4} (S_{\lambda 2})^2} \tag{3}$$

in which $S_{\lambda 1}$ and $S_{\lambda 2}$ represent the OSA measurement resolutions of the two consecutive valleys, respectively. Determined from the performance specifications of a particular OSA instrument, $S_{\lambda 1}$ and $S_{\lambda 2}$ are equal ($S_{\lambda 1}=S_{\lambda 2}=S_\lambda$) since the instrument has a consistent measurement resolution of wavelength within the specified observation bandwidth. In addition, within a relatively small observation spectrum range, both λ_1 and λ_2 can be approximated by the center wavelength of the range, λ_0. As a result, Equation 3 can be simplified into:

$$S_l \approx S_\lambda \frac{{\lambda_0}^2}{\sqrt{2}(\Delta\lambda)^2} \tag{4}$$

where $\Delta\lambda$ is the wavelength difference between the two consecutive valleys. For the estimation of measurement errors, $\Delta\lambda$ at a given cavity length can be considered to be a constant within the wavelength bandwidth of observation, though $\Delta\lambda$ slightly increases with wavelength. Equations 2 and 4 indicate that the minimum detectable cavity length decreases in a quadratic manner as $\Delta\lambda$ increases or the cavity length decreases. In other words, as the cavity length increases, the resolution of cavity length or strain measurement becomes lower.

Phase Tracking Method Based on the two beam interference theory (Taylor 2008), the spectral interferogram reaches its minimum when the phase difference between the two beams satisfies the following condition:

$$\frac{4\pi l}{\lambda_v} = (2m+1)\pi \tag{5}$$

where m is an integer that can be estimated following the procedure as specified in Qi et al. (2003), and λ_v is the center wavelength of a specific interference valley. Taking the derivative of the cavity length with respect to λ_v yields

$$\frac{dl}{d\lambda_v} = \frac{2m+1}{4} \tag{6}$$

Therefore, the change in cavity length can be estimated from Equations 5 and 6 as follows:

$$\Delta l = \frac{\Delta\lambda_v}{\lambda_v} l \tag{7}$$

where $\Delta\lambda_v$ is the change in center wavelength of the specific interference valley and Δl is the change in cavity length. As Equation 7 indicates, the cavity length change is directly proportional to the wavelength shift of the interferogram and to the cavity length of the EFPI. Since the minimum $\Delta\lambda_v$ is represented by the instrument measurement resolution or $S_{\lambda 1}$ and $S_{\lambda 2}$, the resolution of the phase tracking method decreases linearly as the EFPI cavity length increases.

Comparison among Three Processing Methods Fig. 3 compares the theoretical strain measurement resolution of three data processing methods when L=*2 mm*. To cover a range of wavelength measurement resolution from various commercial OSAs, let $S_\lambda = \Delta\lambda_v$ be equal to *0.001 nm*, *0.01 nm*, and *0.1 nm*. It can be clearly observed from Fig. 3 that the interference frequency tracking method has constant resolution of approximately *6,000 με*. The resolution of the period tracking method decreases in a quadratic manner as the EFPI cavity length increases. The resolution of the period tracking method is strongly influenced by the resolution of a particular OSA system. If $S_\lambda = \Delta\lambda_v$ = *0.01 nm*, the strain resolution of period tracking method is *600 με*. If $S_\lambda = \Delta\lambda_v$ = *0.1 nm*, the period tracking method has higher resolution than the interference frequency tracking method for l < *320 μm*. In addition, the resolution of the phase tracking method decreases linearly as the EFPI cavity length increases. Among the three methods, the phase tracking method has the highest resolution since it represents the local (most detailed information) change of phase. When l = *320 μm* and the given OSA resolution is *0.1 nm*, the strain resolution of the phase tracking method is *10 με* in comparison with *6,000 με* for the other two methods. However, the phase tracking method can only measure a relatively small change of the cavity length within a 2π phase range to avoid ambiguity. Therefore, its operation range is limited to a change of approximately *0.75 μm* in cavity length or a change of *375 με* in strain. On the other hand, the other two methods can be used to measure a large change of cavity length.

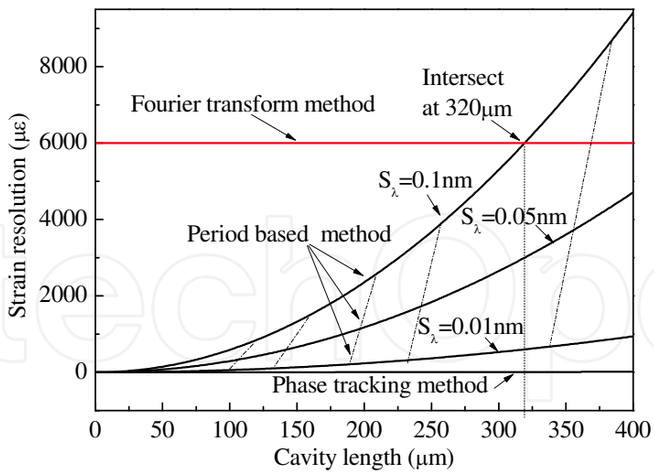

Fig. 3. Resolution as a function of cavity length

2.2 Experiment and discussions

To evaluate the performance of the proposed sensor for large strain measurements, an EFPI-based prototype sensor was constructed with transparent glass tubes so that any change in cavity length can be observed in the laboratory by using an optical microscope as shown in Fig. 2(b). The lead-in side of the fiber sensor was fixed on an aluminum block and the fiber mirror side of the sensor was attached to a computer-controlled precision stage so that the cavity length can be controlled precisely. The gauge length of the strain sensor was set to 2 mm. The reference strain, which will be further discussed in Fig. 5, was determined by dividing the change in cavity length, directly measured by stage movement, by the gauge length. The strain detected by the EFPI sensor is obtained by dividing the cavity length calculated from an EFPI signal to the gauge length.

Fig. 4(a) presents two interferograms of the EFPI sensor prototype with a cavity length of *65 μm* and *175 μm*, respectively. It can be observed from Fig. 4(a) that the interference frequency increases as the EFPI cavity length increases or as more fringes are condensed into a given observation spectrum range. However, the range of interference signal intensities decreases as the EFPI cavity length increases. The signal range is often quantified by a fringe visibility (V) as defined by Equation 8:

$$V = \frac{I_{\max} - I_{\min}}{I_{\max} + I_{\min}} \tag{8}$$

where I_{max} and I_{min} represent the maximum and minimum intensities of an interference signal, respectively. The fringe visibility determined from Equation 8 is plotted in Fig. 4(b) as a function of cavity length. The experiment stopped when the fringe visibility dropped below *20%*, corresponding to a maximum cavity length of approximately *265 μm* of the prototype sensor. The drop in fringe visibility as a function of cavity length was mainly caused by the divergence of the output beam from the lead-in fiber, which was governed by the numerical aperture (NA) of the fiber (Han et al. 2004). Other potential factors such as misalignment are negligible in this study since the glass tubes of the three-layer sensor prototype were assembled with a tight tolerance.

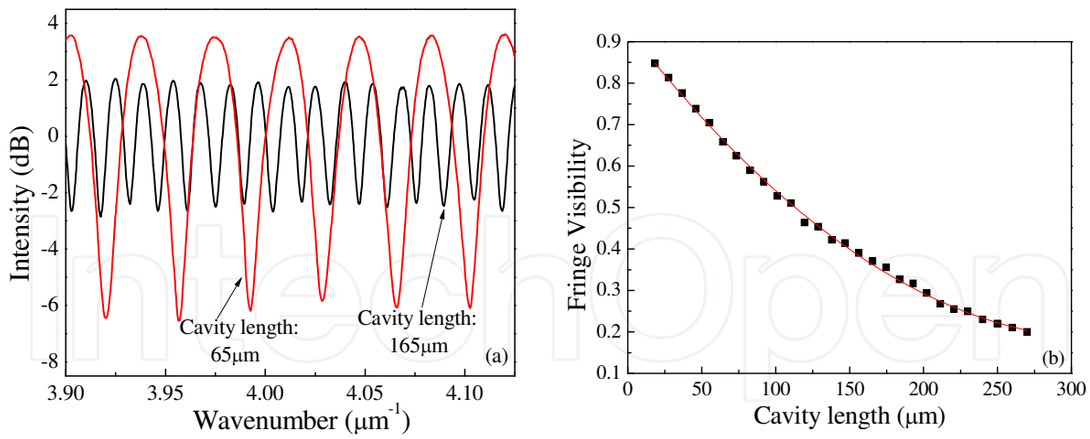

(a) Interferograms with a cavity length of 65 μm and 175 μm

(b) Fringe visibility as a function of cavity length

Fig. 4. Interferogram and fringe visibility

To investigate the measurement resolution of the interference frequency tracking method, large strain measurement experiments were designed and executed. During various tests, the cavity length of the sensor prototype ranged from *15 μm* to *265 μm* at *10 μm* intervals. The maximum change of cavity length was approximately *250 μm*, corresponding to a dynamic strain range of *12.5%*. Fig. 5 relates the reference strain measured by the change in stage movement to the strain measured by the change in cavity length of the EFPI sensor. The theoretic values were directly calculated based on the stage movement; they follow a straight line with a slope of *1:1* as represented by the solid line in Fig. 5. The experimental data points demonstrated only slight fluctuations around the theoretic line. To compare the measurement resolution of the interference frequency tracking method and the period tracking method, refined experiments were conducted within a strain range of *11,000 με* to *21,000 με*. In this case, the precision stage was moved at *2 μm* intervals, giving rise to a strain change of *1,000 με* between two consecutive measurements. The results from the refined experiments processed with both the interference frequency tracking and period tracking methods are presented as an inset in Fig. 5. It can be seen from Fig. 5 that the theoretical prediction strongly agrees with the test data points that were processed with the period tracking method and the measured strains processed with the interference frequency tracking method follow a zig-zag trend with respect to the theoretic prediction. This comparison indicates that the interference frequency tracking method is unable to resolve a strain difference within an interval of *12 μm* in cavity length. This length resolution corresponds to a strain measurement of approximately *6,000 με*, which agrees with the calculated strain resolution that is limited by the light source bandwidth of *100 nm*.

The relative accuracy between the interference frequency method and period tracking method is supported by Fig. 3 since the cavity length observed during the refined experiments was significantly less than *320 μm* when the two methods had the same resolution. The interference frequency tracking method is advantageous over the other two methods in terms of computational efficiency and constant resolution over the entire dynamic range. In addition, it is immune to localized spectrum distortions that could potentially result in large errors when waveform based signal processing methods are used.

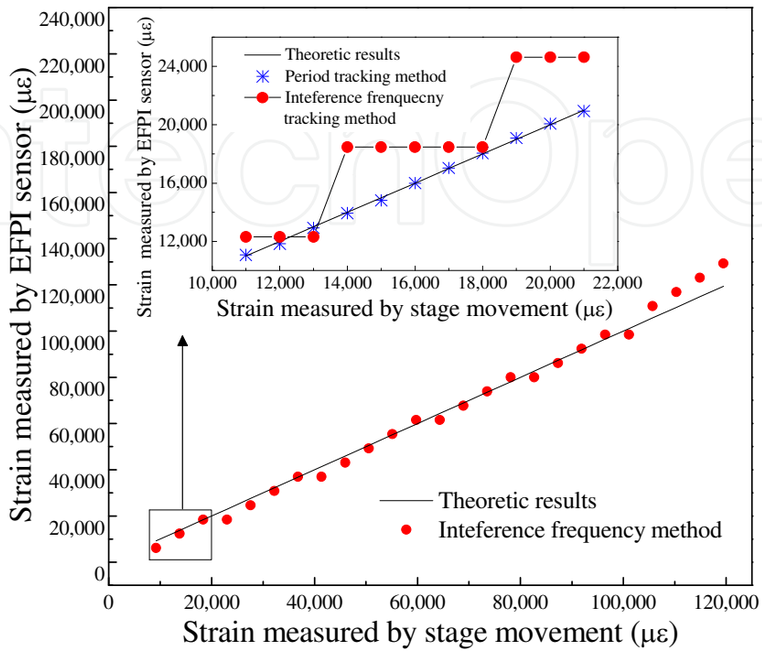

Fig. 5. Measured stains processed with the interference frequency tracking method (inset: comparison between the frequency and period tracking methods)

To verify the accuracy of the phase tracking method, more refined experiments were performed with a smaller stage movement interval of *0.1 μm*. The cavity length of the EFPI sensor was set to range from *15 μm* to 30 μm, which corresponds to a strain of *7,500 με*. Fig. 6(a) shows two representative spectral interferograms of the EFPI sensor at two consecutive stage positions with a cavity length difference of *0.1 μm*. Fig. 6(b) compares the measured strains processed with the phase tracking and the period tracking methods. It can be observed from Fig. 6(b) that the theoretically predicted strain is in agreement with the strain data points processed with the phase tracking method and that of the period tracking method shows a notable deviation from the theoretic prediction based on the reference strains. This comparison indicates that refined resolution can be achieved with the use of the phase tracking method. The maximum deviation of the period tracking method was estimated to be *50 με* at an EFPI cavity length of *30 μm*, which is consistent with the theoretic prediction given in Fig. 3. The deviation is expected to further increase as the EFPI cavity length increases. However, it is worth repeating that the period tracking method can measure a large range of strain while the phase tracking method is limited to a strain measurement range of approximately *375 με*, which corresponds to a phase shift of *2π*.

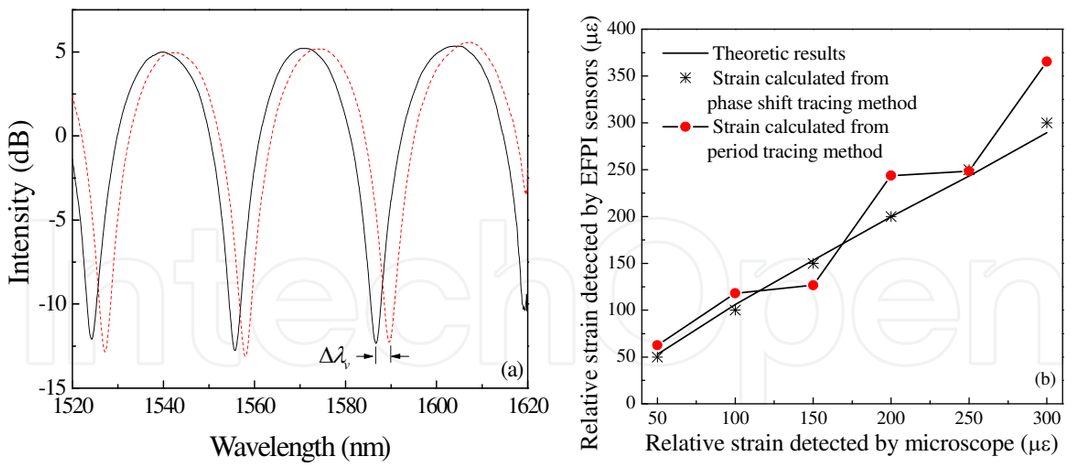

(a) Phase tracking method (b) Period versus phase tracking methods

Fig. 6. Typical spectral Interferograms and strain measurements

3. A quasi-distributed optical fiber sensing system for large strain and high temperature measurements

A hybrid LPFG/EFPI sensor was designed and fabricated by linking a CO_2 laser induced LPFG with a movable EFPI in series. On one hand, LPFG is at least two orders (approximately *100* times) more sensitive to temperature than strain, and thus regarded as a temperature sensing component of the hybrid sensor. On the other hand, packaged with a glass tube only, EFPI has a weak cross effect of temperature on strain measurements in the order of *0.5 με/°C*, depending upon thermal coefficients of the optical fiber and the glass tube. Therefore, EFPI mainly works as a strain sensing component of the hybrid sensor (Huang et al. 2010).

3.1 Sensor structure and measurement system

Built upon Fig. 1(a), Fig. 7 shows the schematic of a hybrid fiber optical LPFG/EFPI sensor structure. The EFPI was formed by two perpendicularly cleaved end faces of a single-mode optical fiber (Corning SMF-28). The left part of the fiber with written gratings (LPFG) serves as a lead-in fiber and the right cleaved end face functions like a low reflective mirror. Both the cleaved end faces were placed inside a capillary tube with an inner diameter of *127 μm* and an outer diameter of *250 μm* to ensure the two end faces move in parallel. One end of the fiber was bonded on the capillary tube and the other end was not. The sensor installation was completed by bonding the capillary tube and the right fiber to a host structure over a gauge length of *L* between the two bonding points. In this study, *L = 2 mm*. The EFPI cavity length was designated as *l*. The bonding between all the components was completed after high temperature tolerable adhesives had been applied (Huang et al. 2008).

Fig. 7 also illustrates the expected main mechanism of light reflection and transmission around a hybrid sensor. As light at the light-in end of the fiber transmits through the LPFG, one part of the light is reflected by the left cleaved end face and the other part is reflected by the right cleaved end face. Since the LPFG is very close to the EFPI, typically less than 5 cm apart, both the EFPI-reflected light beams will be further reflected by the LPFG mirror towards the EFPI. At the light-out end of the fiber, the two branches of secondly reflected lights by the LPFG mirror thus form an interferometer at the OSA output spectrum together

with the spectrum of the LPFG itself. The spatial frequency of the interferometer is only a function of the EFPI cavity length. The refractive index change of the interferometer does not affect the transmission signal of the LPFG itself as a sensor component.

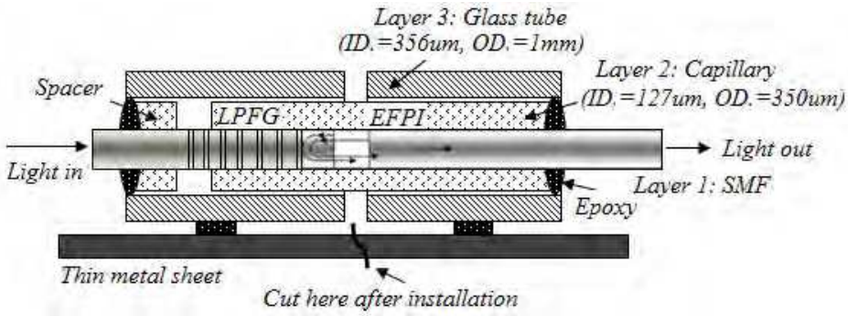

Fig. 7. Sensor structure and operational principle of a hybrid EFPI/LPFG sensor

Fig. 8 shows an optical sensing system of multiple hybrid LPFG/EFPI sensors. Light from a broadband source was channelled through each sensor head by two N-channel D configuration Input/output optic switchers, and received by the OSA. The OSA was then connected to a personal computer for real time data processing. A typical transmission spectrum seen on the OSA is illustrated in Fig. 8 as well. With the two N-channel D configuration optic switchers, N strategic locations of a critical structure can be monitored for simultaneous large strain and high temperature measurements.

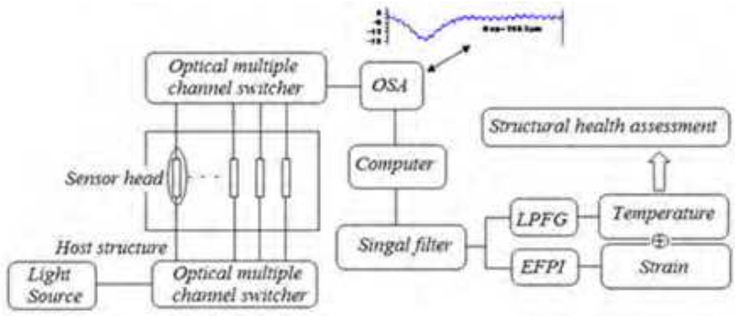

Fig. 8. An optical sensing system of hybrid EFPI/LPFG sensors

3.2 Decomposition of the signal from a hybrid LPFG/EFPI sensor

To enable the decomposition of a recorded signal into components from each LPFG sensor and each EFPI sensor in the hybrid sensing system, LPFG sensors must be designed with different wavelengths for multiplexing and EFPI sensors are given different optical paths. The signal processing algorithm for the signal decomposition is discussed below.

To measure temperature and strain at a specific location of a structure, the distance between the LPFG and EFPI components of a hybrid sensing system must be short, i.e., within *5 cm*. With such a short distance between the two sensor components, the transmission signal of a hybrid sensor approximately represents a combined effect of individual LPFG and EFPI components. Fig. 9(a) illustrates a typical spectral interferogram of the hybrid LPFG/EFPI sensor as detailed in Fig. 7 with a cavity length of over *20 μm*, and Fig. 9(b) shows the phase and amplitude of the Fast Fourier Transform (FFT) of the interferogram. It can be seen from Fig. 9(b) that the spatial frequency of the LPFG component is low and that of the EFPI

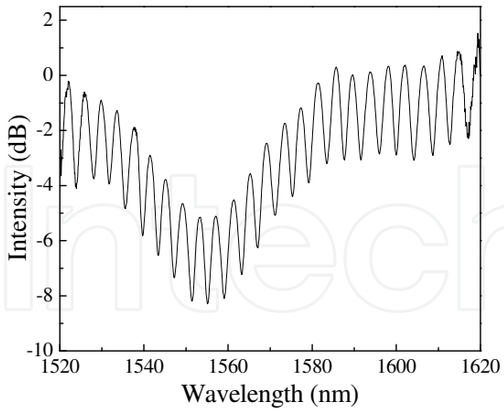

(a) Spectral interferogram of a hybrid sensor

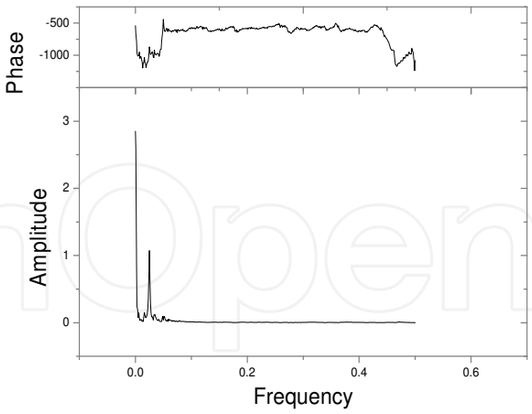

(b) FFT of the hybrid sensor's spectral interferogram

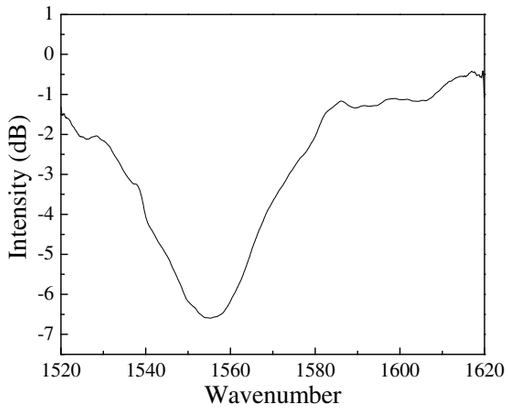

(c) Low-pass spectrum of the LPFG

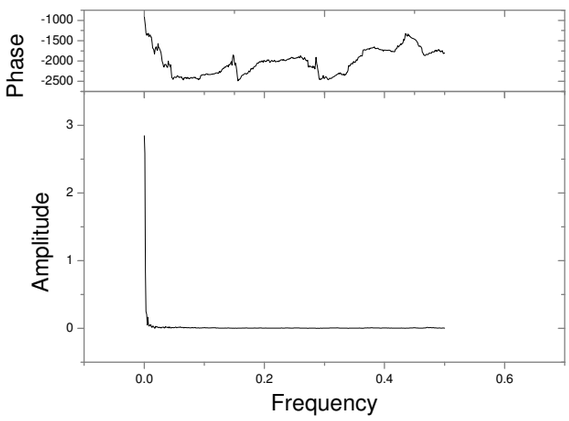

(d) FFT of the LPFG's spectrum

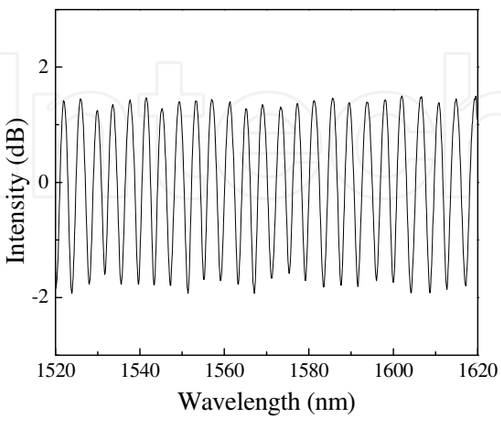

(e) High-pass interferogram of the EFPI

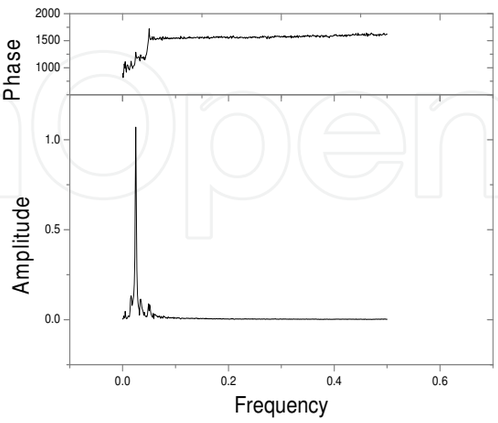

(f) FFT from the EFPI

Fig. 9. Transmission spectra and their FFTs of various sensors with low-pass and high-pass filters

component is significantly higher. Therefore, to decompose the signal into two parts from the LPFG and EFPI components, respectively, a low-pass filter was applied. Figs. 9(c, d) present the spectrum of the LPFG, a low-passed signal from Fig. 9(a), and its Fourier transform. As such, the interferogram of the EFPI was then obtained by subtracting Fig. 9(c) from Fig. 9(a), as shown in Fig. 9(e). Its Fourier transform is presented in Fig. 9(f). The cavity length of the EFPI can be calculated from the decomposed signal based on the spectral frequency tracking method as discussed in Section 2.1.2.

3.3 Experiments and discussions

As indicated in Fig. 5, the EFPI component only of a hybrid LPFG/EFPI sensor can measure a gap distance change of up to *260 μm*, corresponding to a strain of *12%* for a gauge length of *2 mm*, and temperature as high as *1292 °F* (*700 °C*). In this section, a hybrid LPFG/EFPI sensor was tested in the laboratory for simultaneous strain and temperature measurements. The hybrid sensor was installed on two steel channels of *2 mm* apart, which were fixed on two computer controlled precise stages. The steel channels together with the hybrid sensor were further put into the high temperature furnace (made by Thermo Electron Corporation). Figs. 10(a, b) illustrate the measured temperature and strain. The hybrid LPFG/EFPI worked well up to *1292 °F* (*700 °C*) and the difference between the strain calculated from the interference frequency method and that from the movable stage was within *5%*, which is acceptable for large strain measurement. Fig. 10(b) also illustrates that the influence of temperature on the EFPI signal was small and insignificant.

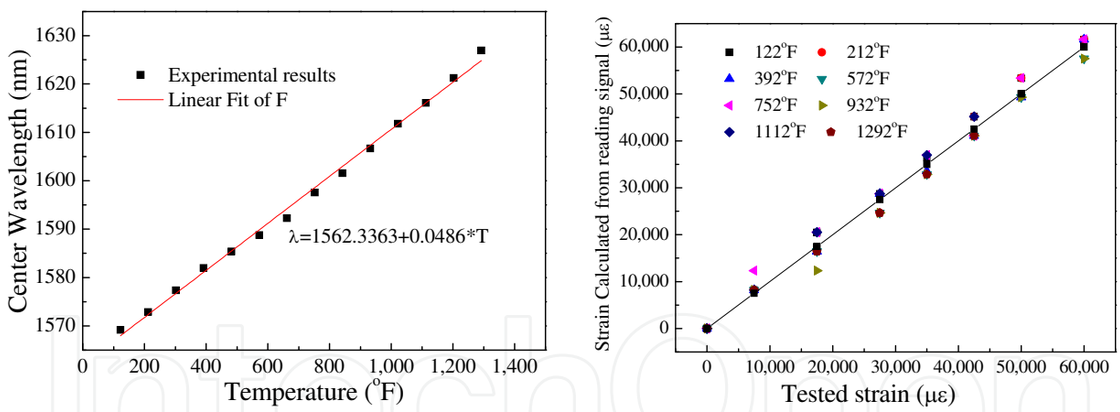

(a) Wavelength change with temperature (b) Strain accuracy and temperature effect

Fig. 10. Temperature sensitivity, cross temperature-strain effect, and strain measurement accuracy of a LPFG/EFPI sensor

4. Post-earthquake assessment of steel buildings under simulated earthquake and fire loadings with an optical fiber sensor network

4.1 Design of an idealized steel frame

A single-bay rigid frame of one top beam and two columns is considered in this study. The frame was made of A36 steel and built with hot-rolled S-shapes as shown in Fig. 11. To illustrate a potential switch of failure modes from one column to another under earthquake and post-earthquake fire loadings, respectively, a substructure of the frame consisting of one

column (#1 in Fig. 11) and the top beam was tested under a static lateral load to simulate earthquake effects and the entire frame with two identical columns was tested with the other column (#2 in Fig. 11) placed in a high temperature environment to represent post-earthquake fire effects. The former is referred to as an L-shaped frame and the latter is referred to as a two-column frame for clarity in the following discussions.

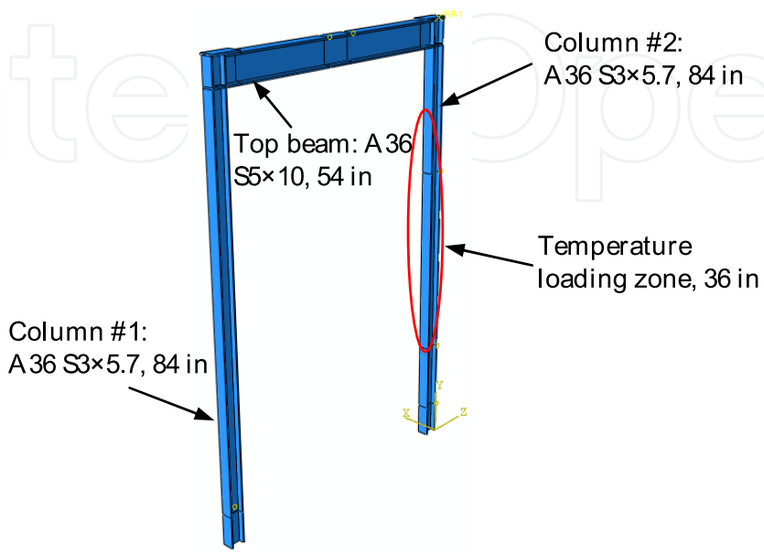

Fig. 11. Rendering of the steel frame

The dimensions of the steel columns were determined based on the size of an electric furnace (Lindberg/Blue M Tube Furnaces) used to simulate the high temperature effect of post-earthquake fires on the progressive collapse of the frame structure. The overall dimension of the furnace used for testing is *22×54×16 in.* (*55.9×137.2×66 cm*) with an actual heating zone of *36 in.* (*91.4 cm*) in length and an inner diameter of *6 in.* (*15.24 cm*). Considering additional spaces required for the assembling (welding of stiffeners, beam-column joint, and column-tube connection) of the two-column frame after column #2 has been placed through the round furnace, the length of the columns was selected to be *84 in.* (*213.4 cm*). To provide a sufficient space for frame deformation at high temperature, the columns of the steel frame were selected as *S3×5.7*, which has a flange width of *3 in.* (*7.62 cm*) and a height of *4 in.* (*10.16 cm*). To design a rigid beam, the stiffness of the top beam was set at least *5* times that of each column. As such, a hot-rolled *S5×10* beam was selected. Since the anchors on the strong floor in the structures laboratory are spaced *36 in.* (*91.44 cm*) apart, the length of the top beam was selected to be *56 in.* (*142.2 cm*), which is equal to the anchor spacing plus the width of one bolted plate on the floor and twice the width of an angle stiffener. To ensure a rigid beam-column connection, three stiffeners were provided on each column: a *3×12×0.5 in.* (*7.62×30.48×1.27 cm*) stiffener placed on the top cross section of the column, and two *1.4×3.9×0.5 in.* (*3.556×9.9×1.27 cm*) stiffeners placed between the two flanges of the column on two sides of the column web, extending the bottom flange of the beam. Stiffeners were welded to the steel frame at the beam-column connection. The overall design of the steel frame is shown in Fig. 11. The column subjected to earthquake effects only is referred to as Column #1 while the other column directly subjected to earthquake-induced fire effects is referred to as Column #2.

4.2 L-shaped steel frame and earthquake-induced damage

4.2.1 Test setup and instrumentation under lateral loading

To simulate earthquake damage of the steel frame (Column #1 only), Column #1 and the top beam was placed on the strong floor and subjected to cyclic loading. Fig. 12 shows the test setup of the L-shaped frame and its prototype in the inset. The L-shaped frame was welded on a steel tube of *6×6×132 in*. (*15.24×15.24×335 cm*) with *½ in*. (*1.27 cm*) wall thickness. In addition, two triangle brackets were individually welded to the two flanges of the column and the square tube to ensure a rigid connection between the column and the tube. The square tube was anchored into the strong floor at four anchor locations. To prevent it from experiencing large deformation, the square tube was stiffened near the base of the column by three stiffener plates of *12×5.5×0.5 in*. (*30.48×13.94×1.27 cm*). The stiffeners were welded on the three sides of the square tube: column base face and two side faces. To approximately represent the two-column frame behavior, the free end of the top beam was transversely restrained by a roller-type support. A cyclic load was applied to the top of the column or the top beam by means of a hydraulic actuator. The applied load was measured by a 5-kip load cell installed between the actuator and the frame. To monitor the structural behavior under the cyclic load, *15* conventional strain gauges were deployed and distributed along the column and the beam as located in Fig. 12. They are designated with a prefix of SG#. For example, SG#1 means the strain gauge #1 that was deployed to monitor the strain in the column-to-tube connection. Similarly, SG#12 was used to assess the beam-column joint condition. In addition, two linear variable differential transformers (LVDTs) were respectively deployed *8 in*. (*203.2 mm*) above the column base and *14 in*. (*355.6 mm*) below the bottom flange of the top beam. LVDT#1 was deployed at the bottom of the column to ensure that the column is not displaced during testing. LVDT#2 was deployed at this location for convenience.

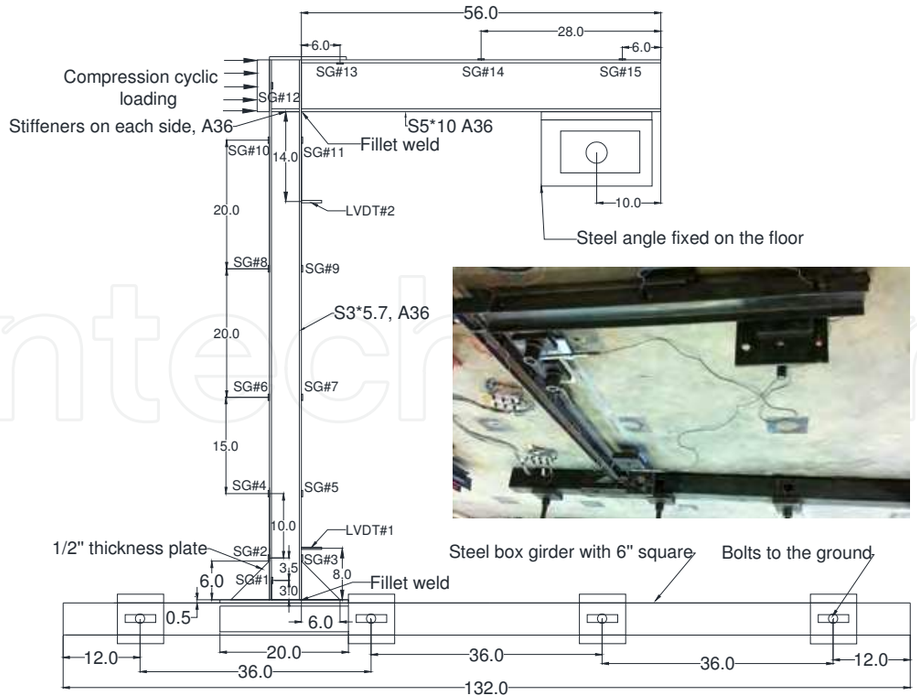

Fig. 12. Test setup and instrumentation of the L-shaped steel frame with a prototype inset (unit: in.)

4.2.2 Loading protocol and simulated earthquake damage

Fig. 13 presents the cyclic loading protocol, measured strains and displacements of the L-shaped frame structure. As shown in Fig. 13(a), five cycles of loading were applied to the frame following a sawteeth pattern. The first four cycles of loading reached *3.4 kips* (*15.1 kN*) at which the column expects to experience initial yielding, and the last cycle reached *3.8 kips* (16.9 kN) to ensure that the column is subject to inelastic deformation. For all cycles, the frame structure was loaded and then unloaded at a rate of *-5.46 lb/sec* (*-24.29 N/sec*) and *-10.92 lb/sec* (*-48.57 N/sec*), respectively.

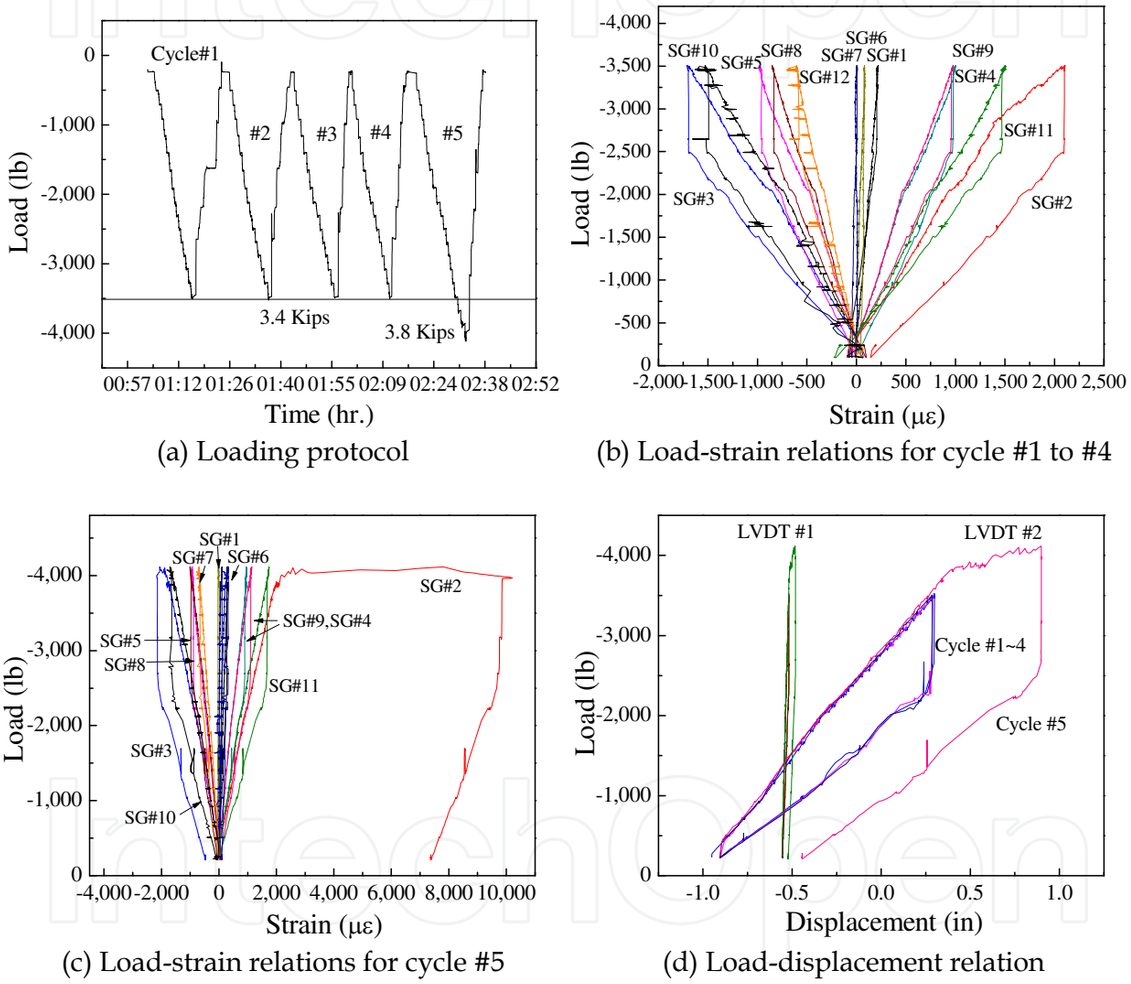

(a) Loading protocol

(b) Load-strain relations for cycle #1 to #4

(c) Load-strain relations for cycle #5

(d) Load-displacement relation

Fig. 13. Cyclic loading, measured strains and displacements

The measured strains (raw data) of the column are presented as a function of the applied load in Fig. 13(b) during the first four cycles of loading and in Fig. 13(c) during the last cycle. For the first four loading cycles, the maximum strain at the bottom of the column (SG#2) was approximately *0.2%*, indicating initial yielding of the test frame. For the fifth cycle, the strain reached *1%* as the load was held at *3.8 kips* (16.9 kN) for a few seconds. After unloading, a permanent strain of *0.75%* remained at the column base (SG#2). Throughout the tests, the maximum strains in the beam-column and column-tube connection areas are

both insignificant due to their significantly stronger designs than that of the column member. The maximum strains at locations slightly away from the connection areas are the highest as shown in Fig. 14 for strain distributions along the height of the column (outside face) during the first four cycles and the fifth cycle of loading. It can be clearly observed from Fig. 14 that Column #1 was subject to double curvatures with a zero strain around *20 in*. (*50.8 cm*) above the column base. The extent of inelastic deformation was mainly limited to the bottom portion of the column during the fifth cycle.

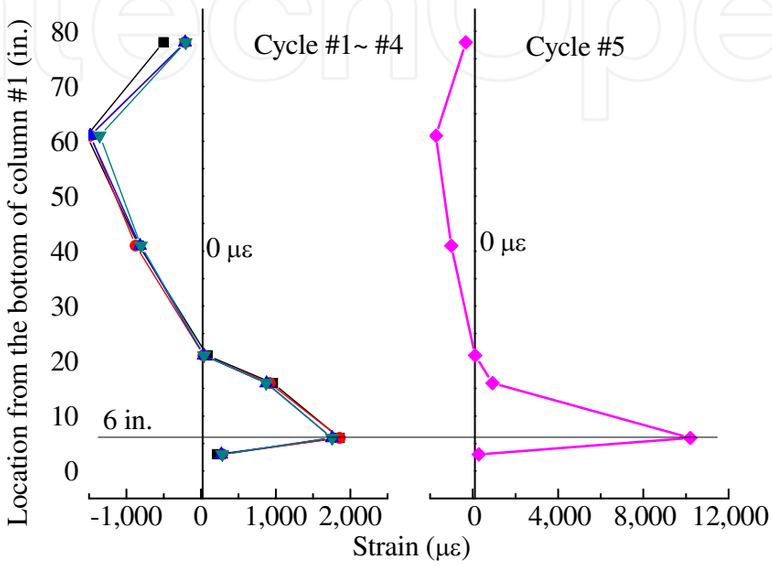

Fig. 14. Distribution of the maximum strains along the column height

The displacement change with load is presented in Fig. 13(d) in various loading cycles. It can be observed from Fig. 13(d) that the displacement change from LVDT#1 is negligible, indicating that the frame base was basically fixed to the strong floor. The largest displacement of *1.8 in*. (*4.572 cm*) was observed at the top of the column (location of LVDT#2), leaving behind *0.5 in*. (*1.27 cm*) permanent deformation in the column when unloaded. The permanent plastic strain and deformation introduced by the cyclic loading represented a large strain condition that can be induced by an earthquake event.

4.3 Two-column steel frame and fire induced damage

4.3.1 Test setup and instrumentation under fire loading

Fig. 15 shows the overall test setup of the two-column frame and various data acquisition systems used during tests as well as side views of the frame (shown in the inset). The frame was fixed to the strong floor at the base of both columns through the same square tube as used for cyclic tests. To simulate the gravity effect, the frame is subjected to a vertical load applied in displacement control by a hydraulic actuator against a rigid reaction beam. One column (#2) passed through a high temperature furnace before it was welded to the remaining L-shaped frame. A wood frame was built as a lateral support for instrumentation. Commercial sensors included *10* K-type thermocouples (TM), *5* high temperature strain gauges (HSG), and *15* strain gauges deployed during the earthquake test. Fiber optical sensors consisted of *1* FBG temperature sensor, *2* LPFG high temperature sensors, *5* EFPI

large strain sensors, and 2 hybrid EFPI/LPFG sensors. As shown in Fig. 16, to protect them from potential damage, the fiber optical sensors on Column #2 were attached to the inside face of its flanges. The FBG and *1* LPFG were placed immediately above the furnace to monitor the temperature and strain at this transition area. The other LPFG sensor was located at the base of Column #1 to ensure a good estimate on the boundary condition. Three out of the five EFPI sensors were placed at the end of the heating zone (*36″* total height) and two were located at the third and two-third points as illustrated in Fig. 16. One hybrid EFPI/LPFG sensor was placed at the bottom of the furnace and the other was at the 2/3 length from the bottom of the furnace together with one EFPI sensor.

To closely monitor the structural behavior of the entire steel frame, other than fiber optical sensors, a comprehensive sensing network of commercial sensors was also developed and applied to the frame structure as illustrated in Fig. 17. As illustrated in an inset in Fig. 17, ceramic adhesives that can endure high temperature up to *2012 °F* were used to attach optical sensors on the inside surface of the column flanges.

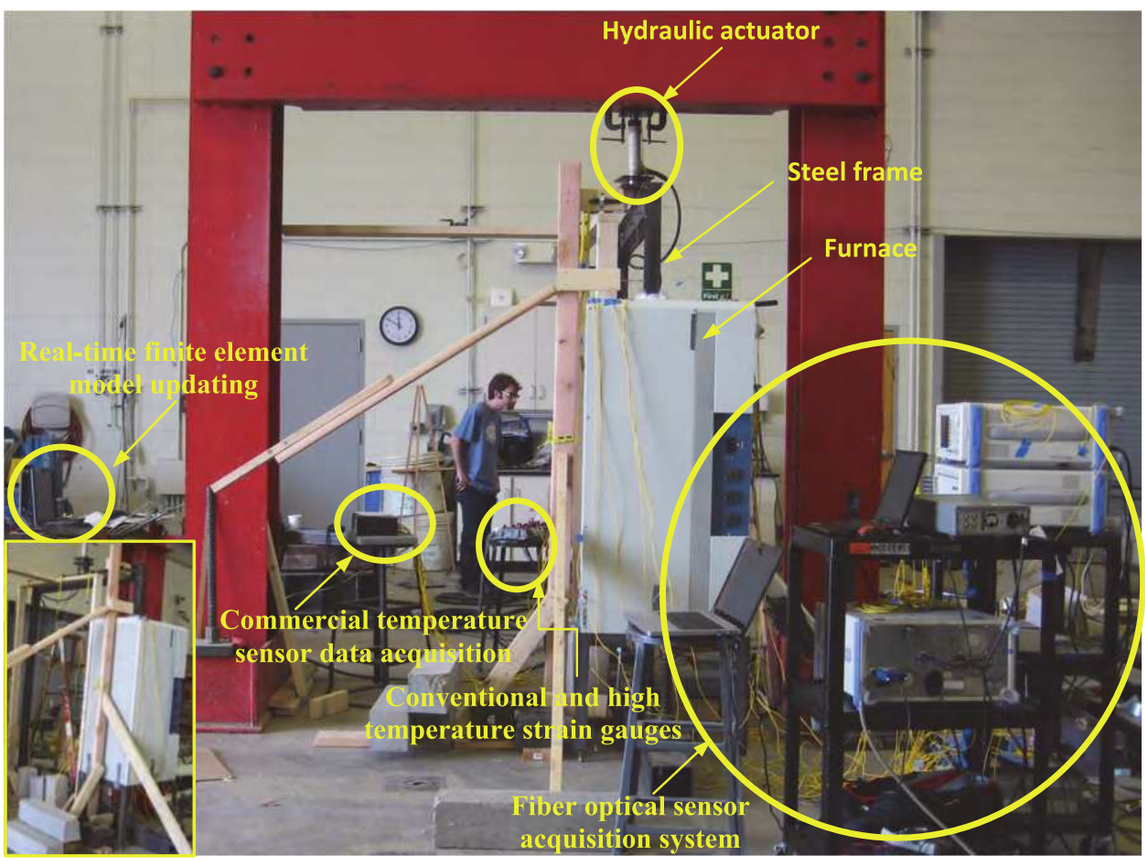

Fig. 15. Overview of the two-column frame test setup and data acquisition systems

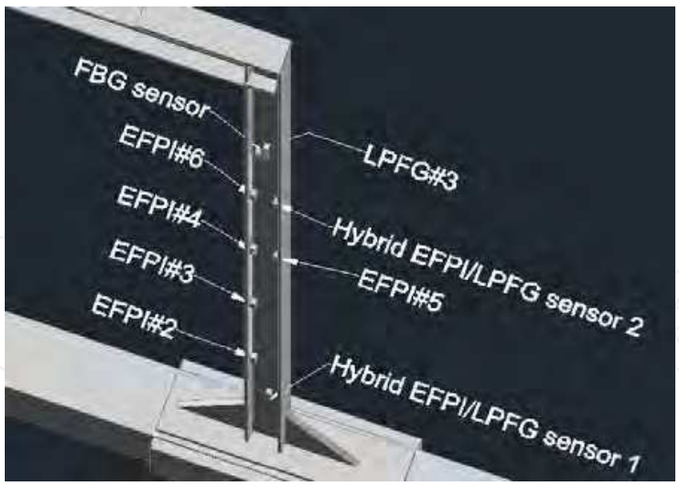

Fig. 16. Specific locations of fiber optical sensors in three-dimensional view

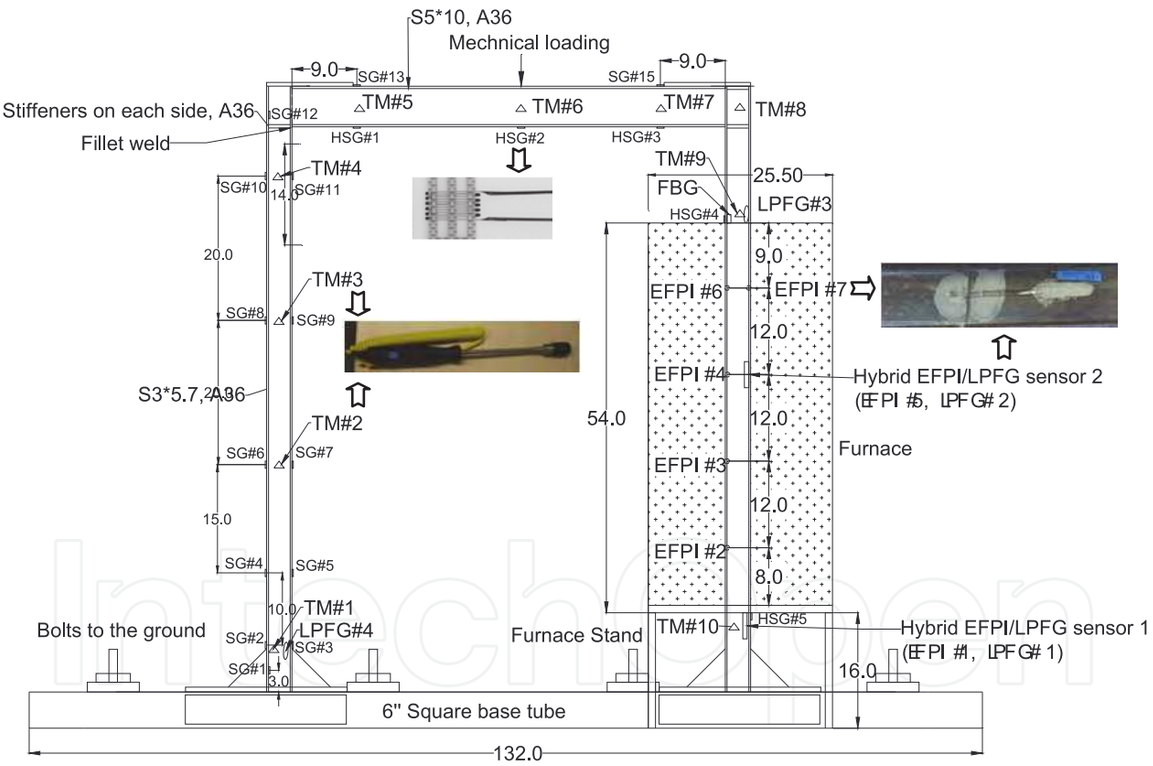

Fig. 17. Instrumentation for simulated post-earthquake fire tests with photos showing the EFPI and hybrid EFPI/LPFG sensors, high temperature strain gauges, and thermocouples

4.3.2 Loading protocol and simulated fire damage

A Lindberg/Blue M tube furnace made by Thermo Scientific was used to provide a high temperature environment that simulates the high temperature effect of a post-earthquake fire. It had three temperature zones that can be programmed and operated independently. In this study, the three temperature zones were programmed to have the same temperature

increase profile. As shown in Fig. 18(a), temperature was increased at a rate of *18 °F/min* from *72 °F* (room temperature, *22 °C*) to *1472°F* (*800 °C*) by an interval of *180 °F* (*100 °C*) or *90 °F* (*50 °C*). At each temperature level, the test paused for *10* minutes to ensure that the temperature distribution is stable both inside and outside the furnace.

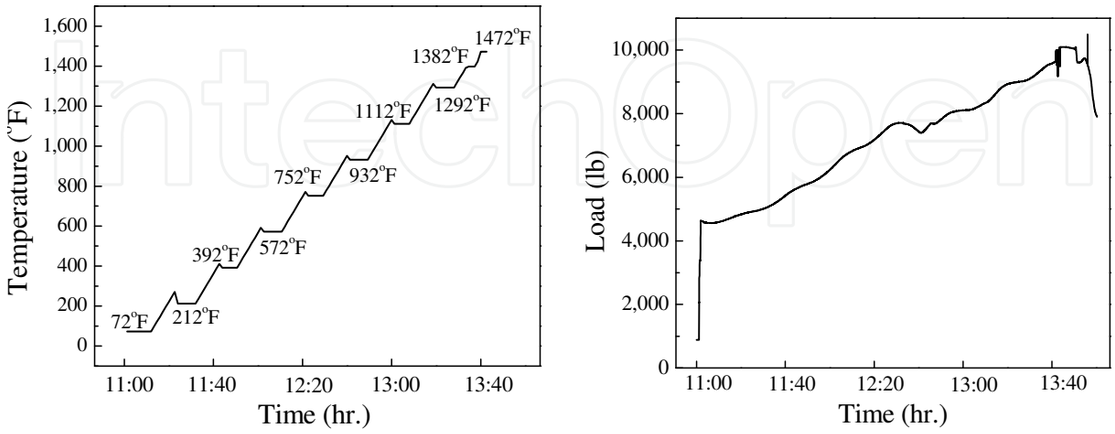

(a) Temperature loading profile (b) Vertical load history

Fig. 18. Loading condition during post-earthquake fire tests

As temperature increased, Column #2 was elongated, increasing the stroke of the hydraulic actuator. As a result, the vertical load applied on the top beam by the displacement-controlled actuator was increased significantly. Corresponding to the increasing of furnace temperature, Fig. 18(b) shows that the frame was subjected to a vertical load of *4.6 kips* (*20.46 kN*) to *10 kips* (*44.48 kN*). Since the applied load was introduced to mainly simulate the gravity effect on the frame structure, an alternate scheme to load the frame needs to be developed in the future to maintain a nearly constant gravity effect.

Fig. 19(a) shows the measured temperatures from *4* LPFG sensors. LPFG#2, which was placed inside the furnace, measured the furnace temperature profile as shown in Fig. 18(a). The temperature on the top of the furnace increased from room temperature to *550 °F* as indicated by the measurement of LPFG#3. Fig. 19(b) shows the measured strains from 7 EFPI sensors after temperature compensation, including those as part of the two hybrid sensors. Note that EFPI#6 and EFPI#7 were malfunctional after strains exceeded *11%*. This is because all EFPI sensors were designed to have the maximum strain of approximately *11%* with an initial cavity of *50~60 μm*. At the top of the heating zone, the steel column is subject to a strain of *8%* at *752 °F* and would have been strained for over *11%* at *927 °F* based on the strain increasing trend over the time. Other locations with maximum strains of less than *11%* were continuously monitored by the EFPI sensors till the end of high temperature tests. It is also observed from Fig. 19(b) that the strains measured by EFPI#4 and EFPI#5 are similar, both slightly larger than that of EFPT#3 for most part. These three sensors were all located inside the furnace. However, the strain measurements by EFPI#2 (bottom of the furnace) were substantially smaller than those from EFPI#6 and EFPI#7 (top of the furnace) even though they were both located at the end of the furnace. This comparison indicated the effect of gravity on the temperature distribution at the boundary of the furnace.

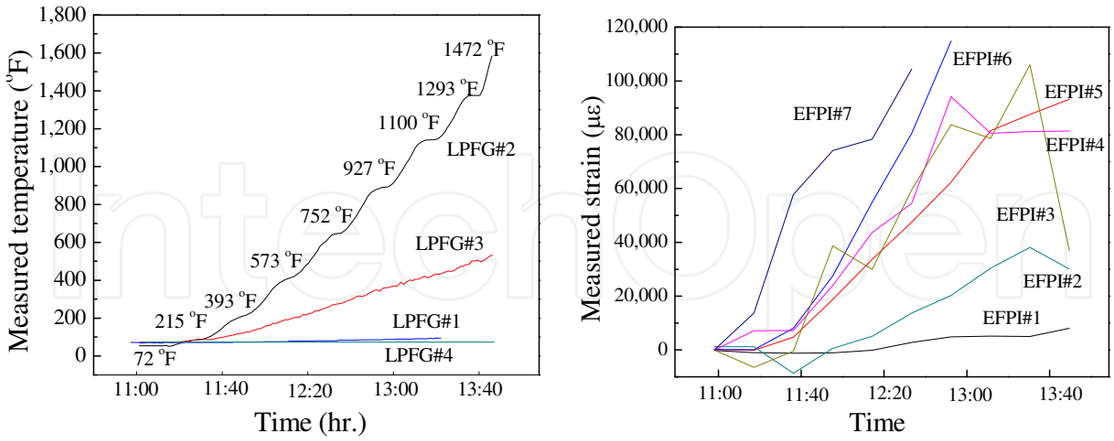

(a) Measured temperature by LPFG sensors (b) Measured strains by EFPI sensors

Fig. 19. Measurements from LPFG and EFPI sensors

By comparing Fig. 13(c) with Fig. 19(b), relative effects of simulated earthquakes and earthquake-induced fires on column stability of the test frame can be discussed. During the cyclic load tests simulating earthquake effects, Column #1 was subjected to approximately *1%* strain or ductility of *8* for A36 steel. This level of strain likely represents the effect of a moderate earthquake. In a post-earthquake fire environment, Column #2 was subjected to over *10%* strain or ductility of over *80* for A36 steel. At *1472 °F*, Column #2 became unstable due to extensive strain and deformation, resulting in a progressive collapse of the steel frame. This was confirmed by a visual inspection of the tested frame towards the completion of the experiment. It can thus be concluded that the fire-induced inelastic deformation of steel structures can far exceed the earthquake-induced deformation under a moderate earthquake event.

To understand how temperature affects the structural condition of the frame outside the furnace, Fig. 20 presents the strain measurements from strain gauges and high temperature strain gauges as the furnace temperature increased. Without direct temperature loading on Column #1, the permanent plastic strain of *0.75%* induced by the simulated earthquake (SG#2) remained nearly constant during the simulated post-earthquake fire condition. The strains at other locations varied little with temperature as well.

4.3.3 Validation of the optical fiber sensing network against conventional sensors

The strains measured by EFPI#1 and HSG#5 are compared in Fig. 21(a) near the bottom of Column #2 immediately below the furnace. The two measurements showed a similar trend with a correlation coefficient of 0.963. This comparison verified the viability of using fiber optical sensors for strain measurements. Similarly, Fig. 21(b) compares various temperature measurements by TM#9, LPFG#3, and FBG sensors near the top of Column #2 immediately above the furnace. Overall they are in good agreement even though the LPFG sensor appeared to give a better comparison with the thermocouple in two temperature ranges as seen in Fig. 21(b).

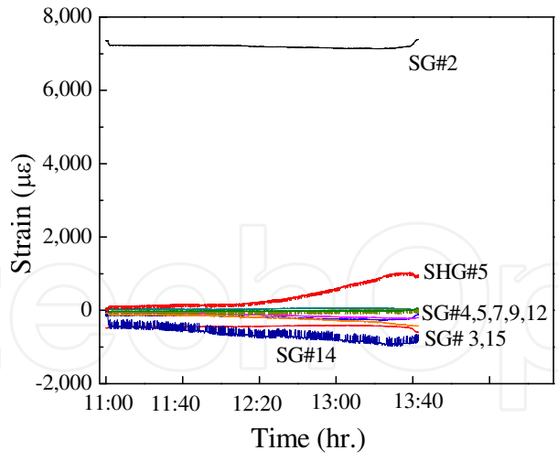

Fig. 20. Change of strains in the frame outside the furnace

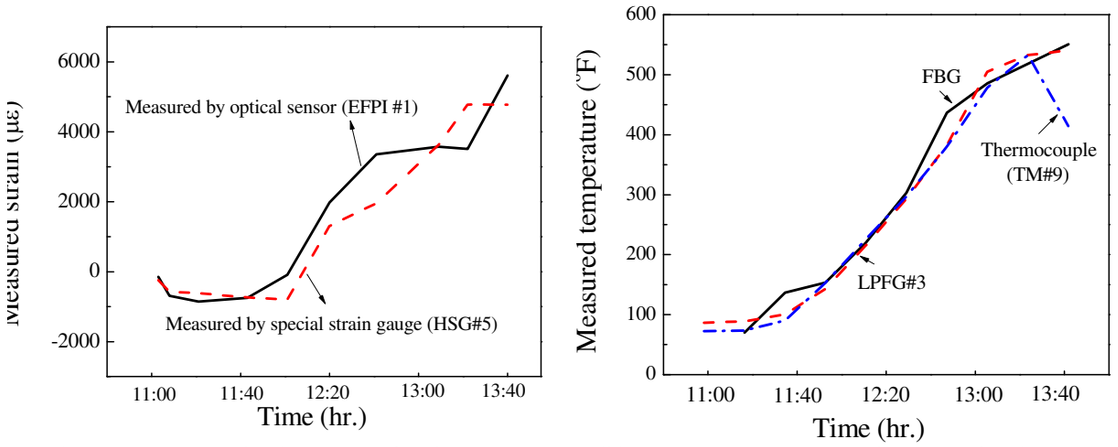

(a) Strains near the bottom of column #2 (b) Temperature near the top of column #2

Fig. 21. Comparison between fiber optical sensors and commercial sensors

5. Conclusions

In this chapter, an optical fiber sensing network of extrinsic Fabry-Perot interferometers and long-period fiber gratings sensors has been developed and validated with laboratory experiments for large strain, high resolution measurements in high temperature environments. The operational principle of the hybrid sensors and three signal processing algorithms were presented, including interference frequency tracking, period tracking, and phase tracking methods. A prototype of the hybrid sensors has achieved strain resolution of *10 με* within a *12%* dynamic range at temperature up to *1472 °F* (*800 °C*). Through extensive tests on a steel frame in a high temperature environment, the developed fiber optical sensors were validated against commercial temperature and strain sensors in their limited measurement ranges; the optical fiber sensing network was proven effective to monitor the structural condition of the frame in real time. On one hand, one column of the two-column frame structure was subjected to significant inelastic deformation during an earthquake event. On the other hand, the other column of the steel structure may experience extensive

strains under post-earthquake fires, resulting in a progressive collapse of the structure. Overall, the developed optical sensing network and fiber optical sensors have been demonstrated to be viable devices for the monitoring and behaviour assessment of steel structures under extreme loads such as earthquakes and earthquake-induced fires. They can be employed in practical applications under harsh conditions.

6. Acknowledgments

Financial support to complete this study was provided in part by the U.S. National Science Foundation under Award No.CMMI-0825942 and by the Mid-America Transportation Centre under Award No. 0018358. The findings and opinions expressed in this chapter are those of the authors only and do not necessarily reflect the views of the sponsors.

7. References

ASTM Committee E20. (1981). *Manual on the Use of Thermocouples in Temperature Measurement (STP-470B),* pp.28-36, ISBN: 0-8031-0502-9, West Conshohocken: ASTM International, 1981

Bhatia, V. & Vengsarkar, A. (1996). Optical fibre long period grating sensors, *Opt. Lett.,* Vol. 21, No. 9, (March 1996), pp.692-694.

Corte, G. D.; Landolfo, R. & Mazzolania, F. M. (2003). Post-earthquake fire resistance of moment resisting steel frames, *Fire Safety Journal*, Vol. 38, No.7, (November 2003), pp. 593-612.

Easerling, K. E. (1963). High temperature resistance strain gauges, *Brit. J. Appl. Phys.,* Vol. 14,No. 2, (February 1963), pp.79-84.

Gregory, O. J. & Chen, X. M. (2007). A low TCR nano-composite strain gage for high temperature aerospace applications, *IEEE Sensors 2007 Conference*, pp.624-627, ISSN 1930-0395, Atlanta, GA, USA, Oct. 28-31 2007.

Habel, W. R.; Hofmann, D.; Hillemeier, B. & Basedau, F. (1996). Fibre sensors for damage detection on large structures and for assessment if deformation behavior of cementitious materials, *Proc. of 11th Engineering Mechanics ASCE-Conference,* pp.355-358, Fort Lauderdale, FL, USA., 19-22 May, 1996.

Habel, W. R. & Hillemeier, B. (1998). Non-reactive measurement of mortar deformation at very early ages by means of embedded compliant fibre-optic micro strain sensors, *Proc. of 12th Engineering Mechanics ASCE-Conference,* pp.799-802, La Jolla, CA, USA., 17-20 May 1998.

Habel, W. R.; Hofmann, D. & Hillemeier, B. (1997). Deformation measurement of mortars at early ages and of large concrete components on site by means of embedded fibre-optic microstrain sensors, *Cement and Concrete Composites,* Vol.19, No.1, (May 1998), pp.81-102.

Han, M. & Wang, A. (2004). Exact analysis of low-finesse multimode fibre extrinsic Fabry-Perot interferometers, *Applied Optics,* Vol.43, No. 24, (August 2004), pp.4659-4666.

Huang, Y.; Chen, G.; Xiao, H.; Zhang, Y.; & Zhou, Z. (2011). A quasi-distributed optical fibre sensor network for large strain and high-temperature measurements of structures, *Proc. SPIE,* Vol. 7983, (March 2011), pp.17-27.

Huang, Y.; Wei, T.; Zhou, Z.; Zhang, Y.; Chen, G. & Xiao, H. (2010b). An extrinsic Fabry–Perot interferometer-based large strain sensor with high resolution, *Meas. Sci. Technol.,* Vol. 21, No. 10, (Sep. 2010), pp.105308.1-8.

Huang, Y.; Zhou, Z.; Zhang, Y.; Chen, G. & Xiao, H. (2010a). A temperature self-compensated LPFG sensor for large strain measurements at high temperature, *IEEE Trans. Instru. & Meas.*, Vol. 50, No.11, (Nov. 2010), pp. 2997 – 3004.

Li, Y. J.; Wei, T.; Montoya, J. A.; Saini, S. V.; Lan, X. W.; Tang, X. L.; Dong, J. H. & Xiao, H. (2008). Measurement of CO_2-laser-irradiation-induced refractive index modulation in single-mode fibre toward long- period fibre grating design and fabrication, *Applied Opt.*, Vol. 47, No.29, (Oct. 2008), pp. 5296-5304.

Liu, T. & Fernando, G. F. (2000). A frequency division multiplexed low-finesse fibre optic Fabry–Perot sensor system for strain and displacement measurements, *Review of Scientific Instruments,* Vol.71, No.3, (Nov. 1999), pp.1275-1278.

Mateus, C. F. R. & Barbosa, C. L. (2007). Harsh environment temperature and strain sensor using tunable VCSEL and multiple fibre Bragg gratings, *2007 SBMO/IEEE MTT-S International Microwave & Optoelectronics Conference*, pp.496-498, ISBN: 978-1-4244-0661-6, Brazil, Oct. 29 -Nov. 1 2007

Othonos, A. & Kalli, K. (1999). *Fibre Bragg Gratings: Fundamentals and Applications in Telecommunications and Sensing,* ISBN-13: 978-0890063446, Boston: Artech House, June 1999

Qi, B.; Pickrell, G. R.; Xu, J.; Zhang, P.; Duan, Y.; Peng, W.; Huang, Z.; Huo, W.; Xiao, H.; May, G. R. & Wang, A. (2003). Novel data processing techniques for dispersive white light interferometer, *Opt. Engrg.,* Vol.42, No.11, (April, 2003), pp. 3165-3171.

Schuler, S.; Habel, W. & Hillemeier, B. (2008). Embedded fibre optic micro strain sensors for assessment of shrinkage at very early ages, *International Conference on Microdurability 2008*, pp.1377-1387, ISBN: 978-2-35158-065-3, Nanjing, China, 13-15 October 2008

Taylor, H. F. (2008). *Fibre Optic Sensor (second edition),* pp. 35-64, CRC Press, ISBN: 1420053655, Boca Raton, 2008

Thomson, W. (1857). On the electro-dynamic qualities of metals, *Proc. R. Soc.,* Vol. 8, pp. 546-50.

Udd, E. (1991). *An Introduction for Scientists and Engineers, Fibre Optic Sensors*, New York: John Wiley and Sons, 1991

Vengsarkar, A. M.; Perdrazzani, J. R.; Judkins, J. B.; Lemaire, P. J.; Bergano, N. S. & Davidson, C. R. (1996). Long-period fibre gratings based gain equalizers, *Opt. Lett.,* Vol. 21, No. 5, (March 1996), pp. 336-338.

Wnuk, V. P.; Méndez, A.; Ferguson, S. & Graver, T. (2005). Process for mounting and packaging of fibre Bragg grating strain sensors for use in harsh environment applications, Proc. of SPIE, Vol. 5758, (March 2005), pp. 46-54.

Xiao, H.; Zhao, W.; Lockhard, R. & Wang, A. (1997). Absolute Sapphire optical fibre sensor for high temperature applications, *Proc. SPIE.,* Vol. 3201, (April 1997), pp. 36-42.

Zhang, B. & Kahrizi, M. (2007). High-temperature resistance fibre Bragg grating temperature sensor fabrication, *IEEE Sensors Journal*, (April, 2007), Vol. 7, No.4, pp. 586 – 591.

Zhang, H.; Tao, X. M.; Yu, T. X.; Wang, S. Y. & Cheng, X. Y. (2006). A novel sensate 'string' for large-strain measurement at high temperature, *Meas. Sci. Technol.,* (February 2006) Vol. 17, No. 2, pp.450-458.

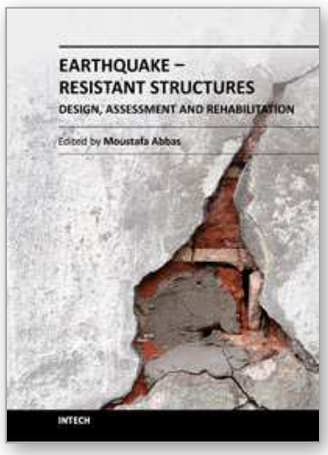

Earthquake-Resistant Structures - Design, Assessment and Rehabilitation

Edited by Prof. Abbas Moustafa

ISBN 978-953-51-0123-9
Hard cover, 524 pages
Publisher InTech
Published online 29, February, 2012
Published in print edition February, 2012

This book deals with earthquake-resistant structures, such as, buildings, bridges and liquid storage tanks. It contains twenty chapters covering several interesting research topics written by researchers and experts in the field of earthquake engineering. The book covers seismic-resistance design of masonry and reinforced concrete structures to be constructed as well as safety assessment, strengthening and rehabilitation of existing structures against earthquake loads. It also includes three chapters on electromagnetic sensing techniques for health assessment of structures, post earthquake assessment of steel buildings in fire environment and response of underground pipes to blast loads. The book provides the state-of-the-art on recent progress in earthquake-resistant structures. It should be useful to graduate students, researchers and practicing structural engineers.

InTech Europe
University Campus STeP Ri
Slavka Krautzeka 83/A
51000 Rijeka, Croatia
Phone: +385 (51) 770 447
Fax: +385 (51) 686 166
www.intechopen.com

InTech China
Unit 405, Office Block, Hotel Equatorial Shanghai
No.65, Yan An Road (West), Shanghai, 200040, China
中国上海市延安西路65号上海国际贵都大饭店办公楼405单元
Phone: +86-21-62489820
Fax: +86-21-62489821

IntechOpen